



Efficiency investigation on energy harvesting from airflows in HVAC system based on galloping of isosceles triangle sectioned bluff bodies

Junlei Wang ^a, Lihua Tang ^b, Liya Zhao ^c*, Zhien Zhang ^d**

^a School of Chemical Engineering and Energy, Zhengzhou University, Zhengzhou 450000, China

^b Department of Mechanical Engineering, The University of Auckland, Auckland, New Zealand

^c School of Mechanical and Mechatronic Engineering, Faculty of Engineering and Information Technology, University of Technology Sydney, 15 Broadway, Ultimo 2007, NSW, Australia

^d William G. Lowrie Department of Chemical and Biomolecular Engineering, The Ohio State University, Columbus, OH 43210, USA

ARTICLE INFO

Article history:

Received 8 August 2018

Received in revised form

26 January 2019

Accepted 1 February 2019

Available online 6 February 2019

Keywords:

Energy harvesting

Galloping

Piezoelectric

Triangular bluff body

ABSTRACT

Galloping-based piezoelectric energy harvester (GPEH) has been used in power generation from small-scale airflows for low-power devices such as Micro-Electromechanical Systems (MEMS) and wireless sensing electronics. The bluff body plays an important role for the onset of galloping. Existing literature regarding analytical and numerical analysis of GPEH has focused on designs incorporating bluff bodies with a variety of cross-sections, such as square, D-section and regular triangle. In this work, a GPEH with triangular cross-section bluff bodies with different vertex angles is investigated. The aerodynamic characteristics are determined by Computational Fluid Dynamics (CFD) and verified by experimental data. Subsequently, an aero-electro-mechanical model with piezoelectric coupling is established and numerically solved. Furthermore, a parametric study is performed to investigate the influence of electromechanical coupling on the GPEH's behavior, with a focus on the threshold wind speed, transverse displacement and power output. It is determined that with weak coupling, the obtuse angle $\beta = 130^\circ$ is the most preferred vertex angle. This is the first documented determination that an obtuse angled isosceles triangle could be used for efficient galloping energy harvesting. The findings provide a guideline for designing efficient GPEHs with triangular bluff bodies.

© 2019 Elsevier Ltd. All rights reserved.

1. Introduction

Micro-Electromechanical Systems (MEMS) and wireless sensor networks (WSNs) have been widely involved in structural health monitoring, industrial sensing and detection, military tracking and environmental surveillance in recent years. However, the limited lifespan and costly replacement of batteries are still challenging issues for sustainable power supply in MEMS and WSNs. On the other hand, harvesting untapped ambient energy from surrounding environment provides an alternative to implement energy-autonomous MEMS and WSNs applications. Studies on energy harvesting from these potential energy sources have been reported in recent years. Energy harvesting from vibrations has been reported in some works, focusing on the low-level energy converted

from ambient mechanical vibrations into electricity using piezoelectric or electromagnetic mechanisms [1–9].

On the other hand, airflow is another energy source abundantly existing in the ambient environment, such as the airflow from heating, ventilation and air conditioning (HVAC) systems, wind gusts around the unmanned aerial vehicles (UAV). "Smart Building" has been considered as an innovative idea in recent decades for intelligent building automation to improve energy efficiency. In building automation applications, if the small-scale airflow energy can be harvested effectively, it can be recovered to power indoor WSNs to save energy while improving the comfort level of occupants at the same time.

Transforming wind energy into mechanical vibration energy is an effective method to enhance the potential of harvesting wind energy, in addition to the conventional rotational motion-based method using wind turbines. Recently, Francesco and Konstantinos [10] presented a concept of high efficiency energy harvesting device with an application for the sustainability of smart building. They tested the device with two different shapes of bluff bodies in

* Corresponding author.

** Corresponding author.

E-mail addresses: liya.zhao@uts.edu.au (L. Zhao), zhang.4528@osu.edu, zhienzhang@hotmail.com (Z. Zhang).

the wind tunnel which emulated the HVAC system. Aeroelastic instabilities are the mechanisms that can be utilized to convert wind energy into vibrations, including vortex induced vibrations (VIV), flutter, translational galloping, wake galloping and torsional divergence [11]. A growing number of studies have investigated the feasibility of harvesting the VIV energy of circular cylinders [12–17]. For VIV energy harvesters, the flow speed range for effective power generation requires the matching between the frequency of vortex shedding and the natural frequency of the VIV harvester. Thus, it is more common to be used in hydroenergy harvesting. For flutter energy harvesting, Li et al. [18] developed a bioinspired piezoleaf architecture to generate electricity via cross-flow fluttering motions. Kwon et al. [19] investigated a T-shaped cantilever to induce flutter oscillations. Other researches focus on flutter energy extraction from flapping foils. Simpson et al. [20] experimentally studied the foils with both sinusoidal sway (heave) and yaw (pitch) motion. Kinsey et al. [21] fabricated and tested a hydrokinetic turbine with oscillating hydrofoils. In addition, galloping is another typical aeroelastic instability of flexible, lightly damped structures with certain cross-sections, given that the wind speed exceeds a critical value, i.e., the cut-in wind speed. The advantage of galloping makes it a better choice to achieve structural vibrations for the purpose of energy harvesting on account of its ability to oscillate in infinite wind speed range over VIV and larger amplitude than flutter.

Barrero-Gil et al. [22] for the first time analyzed theoretically the potential use of transverse galloping to harness energy using a single degree-of-freedom (SDOF) model. For galloping piezoelectric energy harvesting (GPEH), Sirohi and Mahadik [23] proposed an energy harvester consisting of an equilateral triangular bluff body attached to two piezoelectric cantilevers which provided a maximum power of 53 mW at a 4.92 m/s wind speed. They [24] also designed another energy harvester with a D-shaped bluff body connected in parallel with a piezoelectric cantilever. Both linear and nonlinear theoretical analyses were studied recently in the literature, with the performance of the GPEH models being evaluated with a pure resistor. At the same time, equivalent circuit models (ECM) were developed in some studies for piezoelectric energy harvesting from base vibrations, which could address the modeling challenge for systems with complex interface circuits [25]. Unfortunately, for modeling the complex coupling in the GPEH system, the fluid-structure interaction and the complex coupling of practical interface circuit should be taken into account. More recently, some researchers [26] proposed an ECM for GPEH with the aero-elastic force represented by a user-defined component, which could provide the possibility of evaluating the performance of GPEH with complex interface circuits by the system-level circuit simulation. Also, increasing efforts have been devoted into power enhancement of GPEH through interface sophistications [27]. Energy harvesting from concurrent wind flows and base vibrations have also been studied using linear GPEH [28] and modified impact-based bilinear GPEH systems [29].

On the other hand, since the noncircular shape of bluff body for a GPEH is important during energy harvesting, many shapes of cross-sections have been studied recently: square, equilateral triangle, D-shape, etc. Yang et al. [30] experimentally compared different tip cross-sections for small-scale wind energy harvesting. However, isosceles triangular section for GPEH has rarely been reported. There is a lack of understanding on the role that vertex angle plays in the oscillating frequency and amplitude during galloping concerning GPEH with isosceles triangular sections.

In this study, the instabilities of cross-flow translational galloping of triangular cross-section bodies have been systematically analyzed through a CFD method and semi-empirical model. The aero-electro-mechanical model is then established with

nonlinear galloping aerodynamic forces calculated from CFD. Sixteen triangular cross-section models are studied with the vertex angle β varying from 10° to 160° in the increment of 10° . Results from the literature are employed to verify the computational aerodynamic force coefficients. Parametric study is performed to investigate the influence of electromechanical coupling on the GPEH's behavior in terms of the threshold wind speed, transverse displacement and power output. To our best knowledge, this is the first study on GPEH using triangle-sectioned bluff bodies with obtuse angles where CFD technology is utilized to simulate the aerodynamic force response. By compromising the sensitivity of galloping threshold and good capacity of harvesting energy with weak coupling, $\beta = 130^\circ$ is determined to be the most preferred vertex angle. It should be noted that this most preferred vertex angle β_m is determined through a parametric study where the vertex angle is roughly swept at an interval of 10° . It is not the exact "optimal" value but the best choice within the considered range of β . This is the first documented determination that an isosceles triangle with an obtuse vertex angle should be used for efficient galloping energy harvesting. The most preferred vertex angle β_m will vary with load resistance in the circuit when the electromechanical coupling is strong. The findings of this work provide a guideline for designing efficient GPEHs with triangular bluff bodies toward self-powered microelectronics by harnessing wind energy.

2. Aerodynamic dynamic modeling

2.1. Fluid-structure interaction modeling and CFD

An isosceles triangular bluff body subjected to the steady cross-flow of velocity U is shown in Fig. 1. The bluff body has the chord length D_c (the characteristic length) and vertex angle β . The aerodynamic force is $F_y = F_L \cos\alpha + F_D \sin\alpha$, where F_L and F_D are the lift force and drag force on the body, respectively. α is the attack angle. Expressing the aerodynamic force in the dimensionless form gives the aerodynamic force coefficient C_{Fy} as,

$$C_{Fy} = b_1 \alpha + b_3 \alpha^3 + b_5 \alpha^5$$

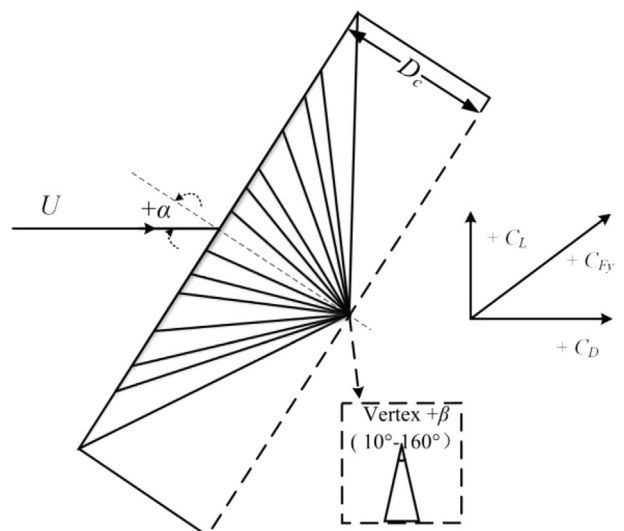


Fig. 1. Configuration of triangular cross-sections and directions of positive quantities.

$$C_{F_y} = F_y(t) / 0.5 \rho_f U^2 S_{tri} \quad (1)$$

where ρ_f is the fluid density and S_{tri} is the characteristic area normal to the fluid flow corresponding to the characteristic length of the bluff body. C_{F_y} is determined by the cross-section shape of the bluff body and the attack angle. The following polynomial expansion is a common way to approximate C_{F_y} :

$$C_{F_y} = \sum_{i=1,2,\dots} b_i(\alpha)^i \quad (2)$$

where b_i ($i = 1, 2, \dots$) is an empirical coefficient for the polynomial fitting based mainly on a Least Square (LS) Method. For galloping, C_{F_y} is usually corresponding to the transverse vibrational displacement. To determine the empirical coefficients of C_{F_y} , an orthogonal distance regression fitting method is utilized to deal with the results. Barrero-Gil et al. [22] summarized the fitting results of C_{F_y} based on the results presented in the literature [31]. Unfortunately, in their work, only three orders were considered. In this work, a fifth-order polynomial is used for curve fitting and equation (2) can be expanded as:

$$C_{F_y} = b_1 \alpha + b_3 \alpha^3 + b_5 \alpha^5 \quad (3)$$

In the literature [31,32], researchers experimentally investigated the aerodynamic coefficient of C_{F_y} with different attack angles to study the galloping instabilities. The flow around a fixed bluff body was investigated and the results of the aeroelastic force coefficients C_L and C_D of the triangular bluff body with vertex angles ranging from 10 to 90° has been obtained in an increment of 10°. In this work, a CFD code is used to get more comprehensive results for a larger range of attack angle between 10 and 160°, that is, the obtuse angles are also considered to investigate the possibility to enhance energy harvesting.

The CFD code is produced based on the Opensource platform OpenFOAM. OpenFOAM solves the continuum mechanics problems by a finite volume discretization method (FVDM) which is composed of C++ libraries. In this work, for obtaining the aerodynamic force on the bluff bodies, the external flow field is simulated by solving the continuity and the Navier-Stokes equation of incompressible fluid with the supposition that the external flow field is 2D and unsteady. The time-dependent viscous flow can be modeled employing the incompressible and unsteady Reynolds-Averaged Navier-Stokes (URANS) equation in conjunction with the one-equation Spalart-Allmaras (S-A) turbulence model [33]. The second-order Gauss integration scheme with a linear interpolation is used in the governing equations for the divergence, gradient, and Laplacian terms. The second-order backward Euler method is used for time integration. In conclusion, the numerical discretization scheme has a second-order accuracy in space and time. To solve momentum and continuity equations together, a pressure implicit splitting of operators (PISO) algorithm has been introduced. The basic equations of URANS are given as follows:

$$\frac{\partial U_i}{\partial x_i} = 0 \quad (4)$$

$$\frac{\partial U_i}{\partial t} + U_j \frac{\partial U_i}{\partial x_j} = -\frac{1}{\rho_f} \frac{\partial p}{\partial x_i} + \frac{\partial}{\partial x_j} \left(2\nu S_{ji} - \overline{u'_j u'_i} \right) \quad (5)$$

where p is pressure, ν is dynamic viscosity, U_i is the mean flow velocity vector and S_{ij} is the strain rate tensor given by

$$S_{ij} = \frac{1}{2} \left(\frac{\partial U_i}{\partial x_j} + \frac{\partial U_j}{\partial x_i} \right) \quad (6)$$

To solve the unsteady URANS equations for mean-flow properties and potential turbulence flow, the Boussinesq eddy-viscosity approximation is adopted here [34], which relates to the Reynolds stress and the velocity gradient. The quantity $\rho_f \overline{u'_j u'_i}$ is the Reynolds-stress tensor and can be modeled as $-\rho_f \overline{u'_j u'_i} = 2\gamma_t S_{ij}$, where γ_t is the turbulence eddy viscosity.

In S-A model, the turbulence eddy viscosity γ_t can be expressed as:

$$\gamma_t = \rho_f \tilde{v} f_{v1} \quad (7)$$

where \tilde{v} is a working variable of the turbulence model depending on the transport equation (8).

$$\begin{aligned} \frac{\partial \tilde{v}}{\partial t} + U_j \frac{\partial \tilde{v}}{\partial x_j} &= e_{b1} \tilde{S} \tilde{v} - e_{w1} f_w \left(\frac{\tilde{v}}{d} \right)^2 + \frac{1}{\sigma} \left\{ \frac{\partial}{\partial x_j} \left[(\nu + \tilde{\nu}) \frac{\partial \tilde{v}}{\partial x_j} \right] \right\} \\ &\quad + e_{b2} \frac{\partial \tilde{v}}{\partial x_i} \cdot \frac{\partial \tilde{v}}{\partial x_j} \end{aligned} \quad (8)$$

$$f_{v1} = \frac{\vartheta^3}{\vartheta^3 + c_{v1}^2} \quad \vartheta \equiv \frac{\tilde{v}}{\nu} \quad (9)$$

where ϑ is an intermediate value, and c_{v1} equals to 7.1 [33]. The details of the transport equation (8) and the definition of parameters can be found in the literature [33], and this approach has been adopted in the work of Ding et al. [34] as well.

2.2. CFD validation

The near-wall grid space is selected to produce a dimensionless wall distance y plus (y_+) between 20 and 30 depending on the Reynolds number. In order to achieve a convergent and accurate solution in a reasonable computational time, three different grid densities are considered in this paper. The grid parameters and selected results are listed in Table 1. The time-average value of the drag coefficient C_D and the root mean square (RMS) value of the lift coefficient C_L are used for the grid independence verification. S_t denotes the Strouhal number.

As shown in Table 1, the results with three different grid densities are similar. Thus in order to save the cost of computation in this work, the medium grid resolution has been selected, as shown in Fig. 2.

To validate the present CFD approach, we have compared the CFD numerical simulation results with the experimental results in the literature [31]. It is noted that the positive direction is the incoming wind direction facing the top angle, while in the present work, the initial position of the bluff body is the opposite, as shown in Fig. 3. As a result, the aerodynamic force coefficient for a vertex beta β in the present paper should be equal to that of the angle (180° - β) in the reference. The computational parameters are the same as in the literature [31], as listed in Table 2 but the wider range

Table 1
Verification of independence of grid density ($Re = 4000$).

Grid number	C_D	C_L	S_t
Coarse (32414)	2.024	0.745	0.155
Medium (49826)	2.023	0.745	0.154
Fine (70102)	2.026	0.744	0.156

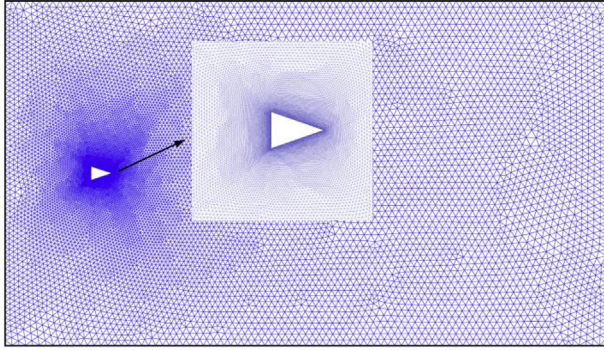


Fig. 2. Computational mesh for isosceles triangular bluff body with $\beta = 30^\circ$.

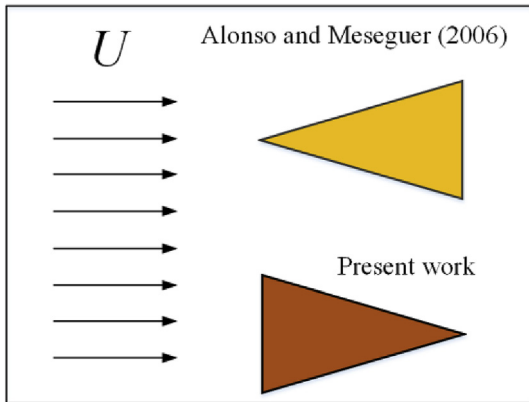


Fig. 3. Schematic of incident wind direction.

Table 2
Aero-elastic computational parameters.

Items	Alonso and Meseguer [31]	Present work
Vertex angle	β [degree]	[10–90]
Characteristic length	D_c [mm]	100
Wind speed	U [m/s]	20
Turbulence intensity	4%	4%

of vertex angle will be considered in the present work.

Fig. 4 compares the responses of lift and aerodynamic drag coefficients resulting from the experiment in the existing literature and current CFD simulation. Fig. 4(a) compares the time-average values of drag force coefficient C_D and lift force coefficient C_L

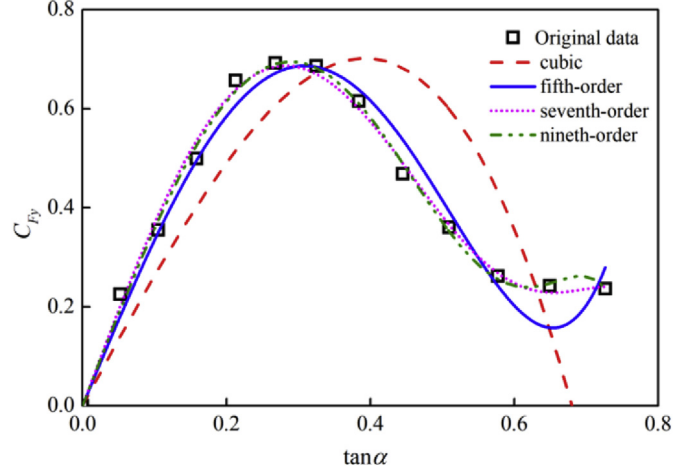


Fig. 5. Comparisons of different polynomial fittings.

under the same operating conditions with the same vertex angle ($\beta = 30^\circ$). It should be mentioned that $-C_D$ instead of C_D is plot for the clarity of presentation in the figure. The polynomial fitting results of the empirical aerodynamic force coefficient C_{Fy} are shown in Fig. 4(b). The plots show that there is a good agreement between the numerical predictions and the experimental measurements in the literature [31].

The comparisons of LS orders for C_{Fy} are shown in Fig. 5. It is noted that the fifth-order fitting is much better than the cubic fitting. Meanwhile, higher orders of fittings are almost indistinguishable. Thus, the fifth-order fitting is a good choice for reasonable accuracy and low computational resources.

2.3. CFD results of C_{Fy} for different bluff bodies

The validated CFD code was then used to compute C_{Fy} for triangular bluff bodies with various vertex angles. The results of aerodynamic force coefficient C_{Fy} are shown in Fig. 6. The coefficients of the fifth-order polynomial, b_1 , b_3 and b_5 , given different vertex angles (β ranging from 10° to 140°) could be derived, as shown in Table 3, in which the results of the obtuse angles are also included.

Fig. 7 shows the vortex shedding patterns of two typical vertex angles $\beta = 100^\circ$ and $\beta = 150^\circ$. When β is not large (i.e. $\beta = 100^\circ$), the vortex shedding pattern shown in Fig. 7(a) demonstrates that the periodic vortex shedding could promise to induce quasi-steady wind-induced vibration. However, when β reaches 150° , i.e., the vertex angle of the isosceles triangular bluff body is too large, the

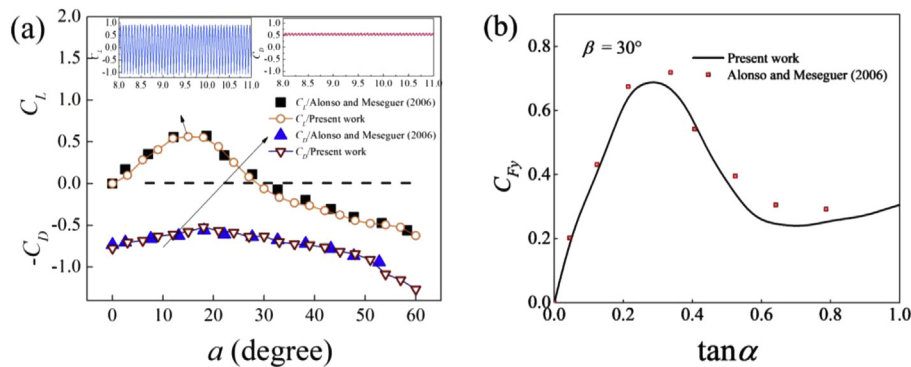


Fig. 4. (a) Comparison of C_L and C_D with vertex angle of $\beta = 30^\circ$ and different attack angles, and (b) comparison of C_{Fy} of present work with experimental data [31].

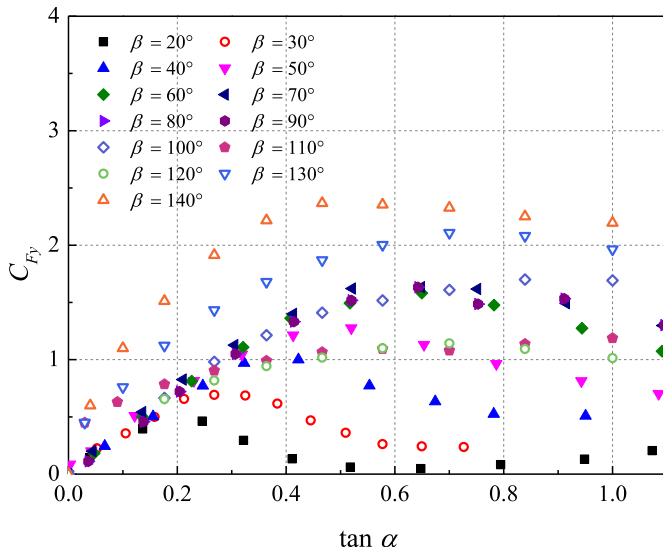


Fig. 6. Aerodynamic force coefficient C_{Fy} for isosceles triangular bluff bodies with different β .

boundary layer at the base angles starts to separate and vortex shedding becomes too weak to induce galloping. The triangular bluff body stalls and the lift coefficient decreases significantly. In other words, triangular bluff body with too large vertex angle is not suitable to induce galloping and thus cannot be used for the purpose of energy harvesting. Hence, they are not included in the present study.

3. Aero-electro-mechanical modeling

Fig. 8 illustrates a practical galloping energy harvester consisting of a bluff body with an isosceles triangular bluff body attached on an elastic cantilever beam at its free end and two piezoelectric elements bonded near its clamped end. The bluff body undergoes galloping when facing the incoming wind, producing an alternating strain on the beam. Meanwhile, the piezoelectric elements deform and produce an electric charge. Thus, AC voltage could be generated in the piezoelectric elements. It is noteworthy that, in the present system, vortex would lead to vibration when GEPH is operated due to the vortex shedding. Fortunately, for non-circular section, galloping is dominant. On the other hand, due to the high wind speed, the lock-in region would not occur in present work. In addition, the cantilever beam serves as a splitter plate behind the bluff body which could effectively restrain the vortex shedding, further enabling such practical GPEH to gallop and suppress the VIV. Therefore, in this work, the influence of VIV on GPEH has been neglected.

The bluff body is elastically mounted. Only the transverse motion, $y(t)$ is possible. At a particular instant, the velocity of the bluff body is $v \equiv \dot{y}(t)$ downwards. The attack angle α is:

$$\alpha = \tan^{-1}(\dot{y}(t)/U). \quad (10)$$

When $\dot{y}(t)$ is small, the attack angle α could be approximated as:

$$\alpha = \dot{y}(t)/U. \quad (11)$$

In **Fig. 8(a)**, the governing equation of the bluff body is:

$$M\ddot{y}(t) + C\dot{y}(t) + Ky(t) = F_y(t) \quad (12)$$

where M is the mass of the bluff body, C is the mechanical damping

Table 3

Fitting coefficients of C_{Fy} of isosceles triangular bluff bodies with different β .

Vertex angle of isosceles triangular bluff bodies β (degree)	b_1	b_3	b_5
10	-0.800	0.971	-0.220
20	2.636	-17.012	26.160
30	3.490	-14.911	17.101
40	3.171	-5.808	2.947
50	2.971	-2.765	0.703
60	3.541	-2.913	0.682
70	3.712	-2.914	-0.677
80	3.477	-2.614	0.595
90	3.601	-2.663	0.602
100	3.241	-1.970	0.425
110	2.370	-1.383	0.257
120	2.530	-1.960	0.466
130	4.651	-3.715	0.977
140	7.032	-9.635	4.032

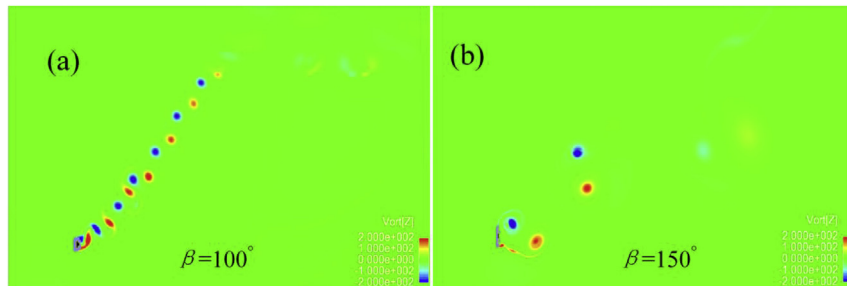


Fig. 7. Aerodynamic characteristics for obtuse vertex angles $\beta = 100^\circ$ and 150° with an attack angle of $\alpha = 55^\circ$: (a) Contour of vorticity for $\beta = 100^\circ$, and (b) contour of vorticity for $\beta = 150^\circ$.

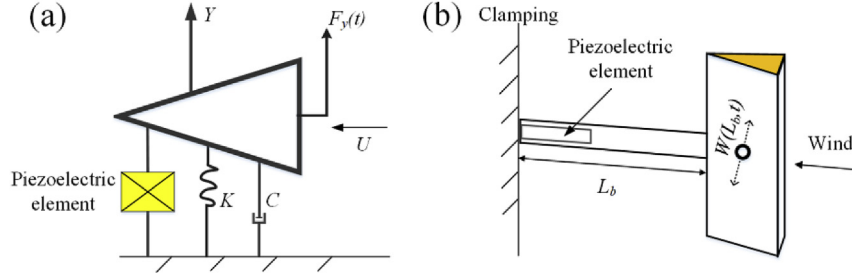


Fig. 8. (a) Lumped single-degree-of-freedom (SDOF) model, and (b) practical cantilevered GPEH design with isosceles triangular bluff body.

coefficient, K is the stiffness of the oscillating system, and the aerodynamic force is $F_y(t) = 0.5\rho_f U^2 S_{tri} C_{Fy}$. $S_{tri} = D_c L_{tri}$ is the windward area (perpendicular to the incoming wind), where D_c is the characteristic length of the triangular section bluff body and L_{tri} is the length of the bluff body.

Equation (12) can be rearranged if $F_y(t)$ is moved to the left-hand-side to group in the damping term as:

$$M\ddot{y}(t) + \left\{ C - 0.5\rho_f U S_{tri} \left[\sum_{i=1,2,\dots} b_i (\dot{y}(t)/U)^{i-1} \right] \right\} \dot{y}(t) + K y(t) = 0 \quad (13)$$

In equation (13), it is noted that when the wind speed U is low, the system is controlled by a positive linear damping and always damped to the equilibrium state. However, by increasing the wind speed, the linear damping will turn negative at a critical wind speed, which is the so-called cut-in wind speed U_{cr} . The vibration amplitude increases due to the negative damping, but the higher order nonlinear damping terms in equation (13) will limit the amplitude simultaneously and induce the final steady state "limit cycle oscillation". The linear and nonlinear coefficients of the overall damping is

$$\text{linear } C = 0.5\rho_f U b_1 S_{tri} \quad (14a)$$

$$\text{nonlinear } 0.5\rho_f U S_{tri} \left[\sum_{i=2,\dots} b_i (\dot{y}(t)/U)^{i-1} \right] \quad (14b)$$

When the disturbance is small enough, the nonlinear term can be neglected. To obtain the threshold of galloping, recalling (3), we note that b_1 is required to be a positive number. Thus, when the disturbance is small, the overall damping of the system should be negative. Recalling the meaning of cut-in wind speed which makes the damping negative, we can get the cut-in wind speed $U_{cr} = 2C/(b_1\rho_f S_{tri})$. Besides, the nonlinear term in (14b) will lead the overall damping back to zero when the oscillation rises, which ensures the steady state limit cycle oscillations.

To simulate the coupled oscillating system, a lumped SDOF model has been used, as shown in Fig. 8(a). Though distributed parameter models based on Rayleigh-Ritz discretization or exact analytical mode shapes can be found in previous work [35], they can be degraded to the single-mode model as the harvester undergoes galloping oscillates at its fundamental mode.

The governing equations of the aero-electro-mechanical coupled GPEH system can be written as.

$$M\ddot{w}(L_b, t) + C\dot{w}(L_b, t) + Kw(L_b, t) + \chi V(t) = F_y(t) \quad (15a)$$

$$I(t) + C_p \dot{V}(t) - \chi \dot{w}(L_b, t) = 0 \quad (15b)$$

where L_b is the length of cantilever beam, $w(L_b, t)$ is the deflection of the beam at the free end (or in other words the translational displacement of the bluff body), M , C and K are, respectively, the effective mass, damping and the stiffness of the system. Besides, χ is the electromechanical coupling coefficient of the system, and C_p is the total capacitance of the piezoelectric elements connected in parallel. $V(t)$ is the voltage across the piezoelectric elements and $I(t)$ is the current flow into the circuit. It is noted that rotation is considered in the paper, as can be seen in Fig. 8(b). Thus the attack angle in the expression of C_{Fy} should be modified into:

$$\alpha = \frac{\dot{w}(L_b, t)}{U} + w'(L_b, t) \quad (16)$$

where the rotation angle at the free end of the beam should be:

$$w'(L_b, t) = Aw(L_b, t), \quad (17)$$

where A is the ratio of the rotation angle to the transverse displacement at the free end of the beam, which can be determined by a finite element analysis [26]. The aerodynamic force can be rewritten as:

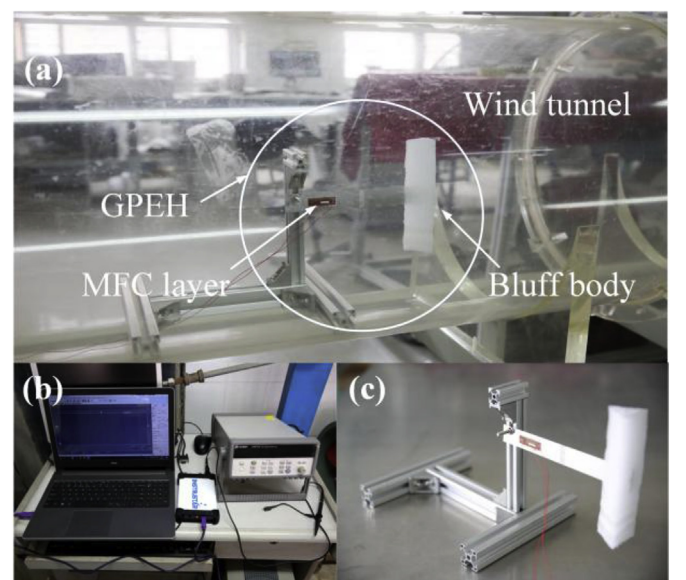


Fig. 9. Experimental setup: (a) overall view of wind tunnel, (b) data acquisition system, and (c) front view of GPEH.

Table 4

Properties of experimental GPEH.

Properties	Cantilever	Piezoelectric sheet
Length (mm)	150	37
Width (mm)	30	11
Thickness (mm)	0.6	0.3
Material/Model	Aluminum	MFC-M2807
Capacitance C_p (nF)	—	15.7

Table 5
Identified parameters of GPEH.

Properties	Value
M	6.27 g
ξ	0.013
f_n	9.6 Hz
C	0.0098 N s/m
K	34.07 N/m
χ	1.183 e-5

$$F_y(t) = 0.5\rho_f U^2 S_{tri} \sum_{n=1,2,3..} b_i \left(\frac{\dot{w}(L_b, t)}{U} + Aw(L_b, t) \right)^{i-1} \quad (18)$$

For equation (15), consider $I(t) = V(t)/R_L$ and introduce the variables as follows,

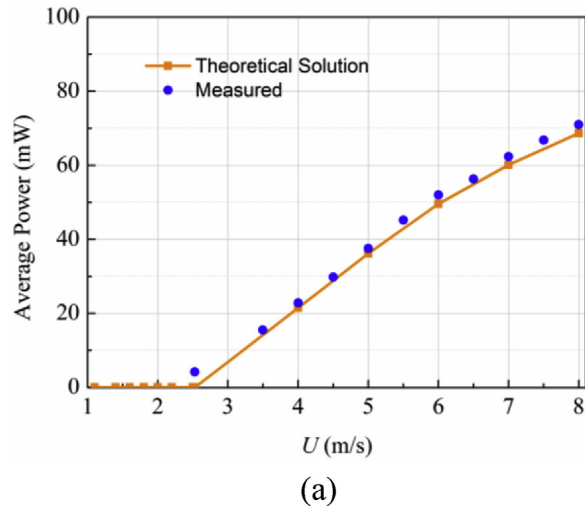
$$\begin{Bmatrix} q_1 \\ q_2 \\ q_3 \end{Bmatrix} = \begin{Bmatrix} w(L_b, t) \\ \dot{w}(L_b, t) \\ V(t) \end{Bmatrix} \quad (19)$$

we can write equation (15) in the state space form as equation (20) and the response of the GPEH can be solved by certain numerical integration tool, for example, the ode45 in MATLAB.

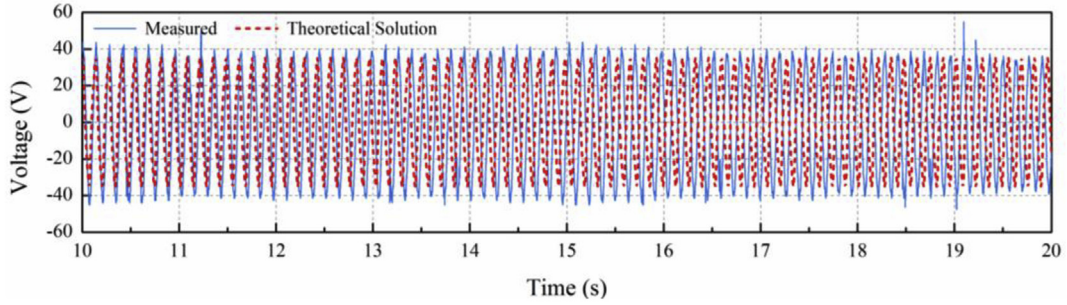
$$\begin{cases} \dot{q}_1 = q_2 \\ \dot{q}_2 = -\frac{1}{M} (Cq_2 + Kq_1 + \chi q_3 - F_y(t)) \\ \dot{q}_3 = \frac{1}{C_p} (\chi q_2 - \frac{q_3}{R_L}) \end{cases} \quad (20)$$

4. Model validation

To validate the present aero-electromechanically coupled model, a GPEH prototype is prepared and tested in the wind tunnel (Fig. 9). The GPEH prototype comprises an aluminum cantilever beam bonded with a piezoelectric transducer (MFC-M2807-P2, Smart Material Corp.) and attached with an equilateral triangular bluff body. The physical parameters of the piezoelectric cantilever beam are listed in Table 4. The piezoelectric transducer is connected to an electrical load resistance (R_L). The frontal characteristic dimension of the equilateral triangular bluff body is 0.032 m. The



(a)



(b)

Fig. 10. Comparison of (a) power output versus wind speed with $R_L = 105 \text{ k}\Omega$, and (b) time history curves of voltage response at $U = 4 \text{ m/s}$ from theoretical solution and experiment.

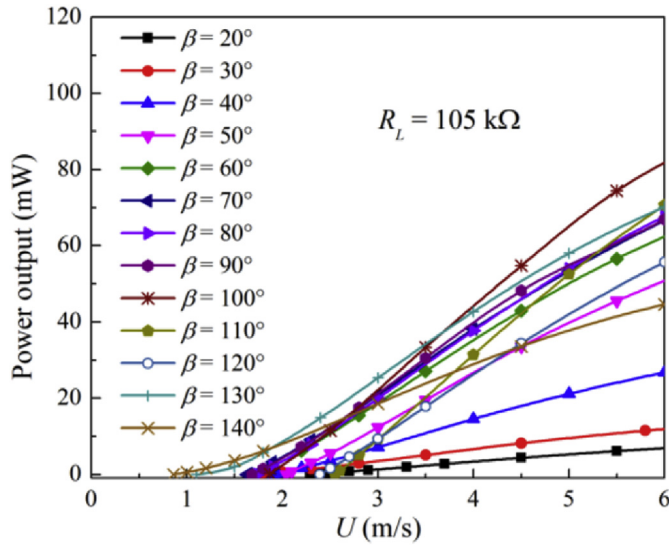


Fig. 11. Power output versus wind speed ($\beta = 20^\circ\text{--}140^\circ$, $R_L = 105 \text{ k}\Omega$).

identified effective parameters of the GPEH is listed in Table 5.

Fig. 10 shows the comparison of the responses of power versus wind speed and the transient voltage response at $U = 4 \text{ m/s}$ with $R_L = 105 \text{ k}\Omega$. As shown in Fig. 10, in general, a good agreement between theoretical results and experimental data can be obtained, though the measured data is slightly higher than the theoretical prediction. The discrepancy is probably attributed to the error of the aerodynamic force coefficient of the bluff body computed by CFD and used in the galloping model, which could be slightly different due to some degree of uncertainty in the experiment.

5. Results and discussion

5.1. Effect of bluff body vertex angles and weak electromechanical coupling

A parametric study of GPEH with different bluff body vertex angles is conducted with the properties $M = 0.02816 \text{ kg}$, $K = 55.72 \text{ N/m}$, $C = 0.0121 \text{ N s/m}$, $\chi = 0.000374$, $C_p = 180 \text{ nF}$. Firstly, in order to determine the most preferred vertex angle β_m for the GPEH design, the power outputs of the GPEH for different wind speeds U under a fixed load resistance R_L are investigated in weak electromechanical coupling condition as shown in Fig. 11. For weak

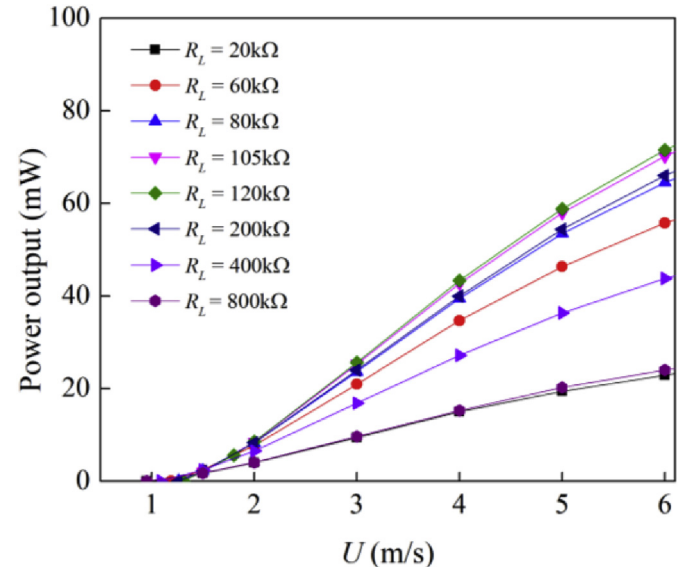


Fig. 13. Power output with different R_L for weak electromechanical coupling ($k_e^2/\zeta = 2.78$).

coupling system, a theoretical optimal load resistance can be estimated as follows [35]:

$$R_{opt} = \frac{1}{\omega_n C_p} \quad (21)$$

In the present system, $R_L = 105 \text{ k}\Omega$ is the optimal load resistance. Fig. 11 shows that the threshold galloping speed U_{cr} of $\beta = 140^\circ$ is the lowest as compared to others. However, the growth rate of power, i.e., the slope of the power response curve is small. On the other hand, the growth rate of power is the highest for $\beta = 100^\circ$, but U_{cr} is also increased as compared to 140° . Considering the real applications in small air flow scenarios ($\leq 5 \text{ m/s}$), $\beta = 130^\circ$ is a good choice to compromise U_{cr} and power at or below 5 m/s.

Figs. 12 and 13 present a further investigation to the influence of load resistance on energy harvesting performance in the weak coupling system with $\beta = 130^\circ$. The parameter k_e^2/ζ is employed to indicate the strength of electromechanical coupling, where k_e is the dimensionless electromechanical coupling coefficient defined as $k_e^2 = \chi^2/(KC_p)$. k_e^2/ζ has been proved to be the critical parameter to indicate the applicable region of synchronized charge extraction interface in vibration piezoelectric energy harvesting [35].

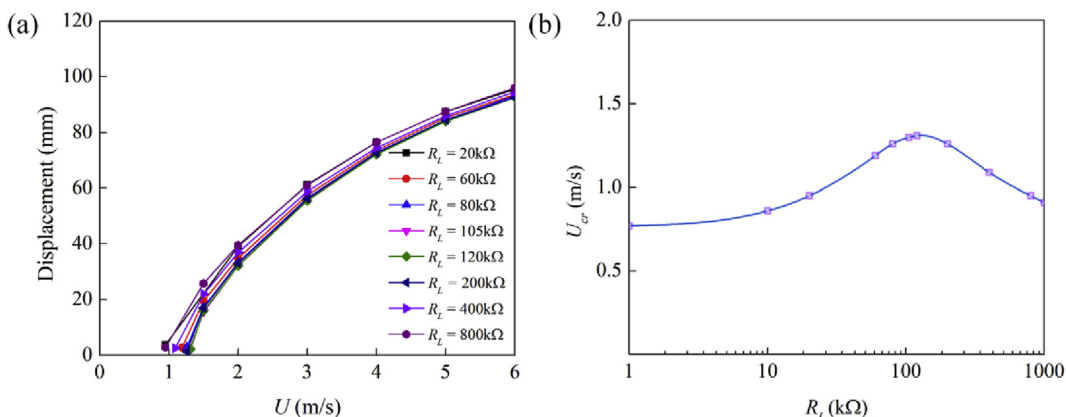


Fig. 12. (a) Displacement versus U with different R_L , and (b) U_{cr} with different R_L for weak electromechanical coupling ($k_e^2/\zeta = 2.78$).

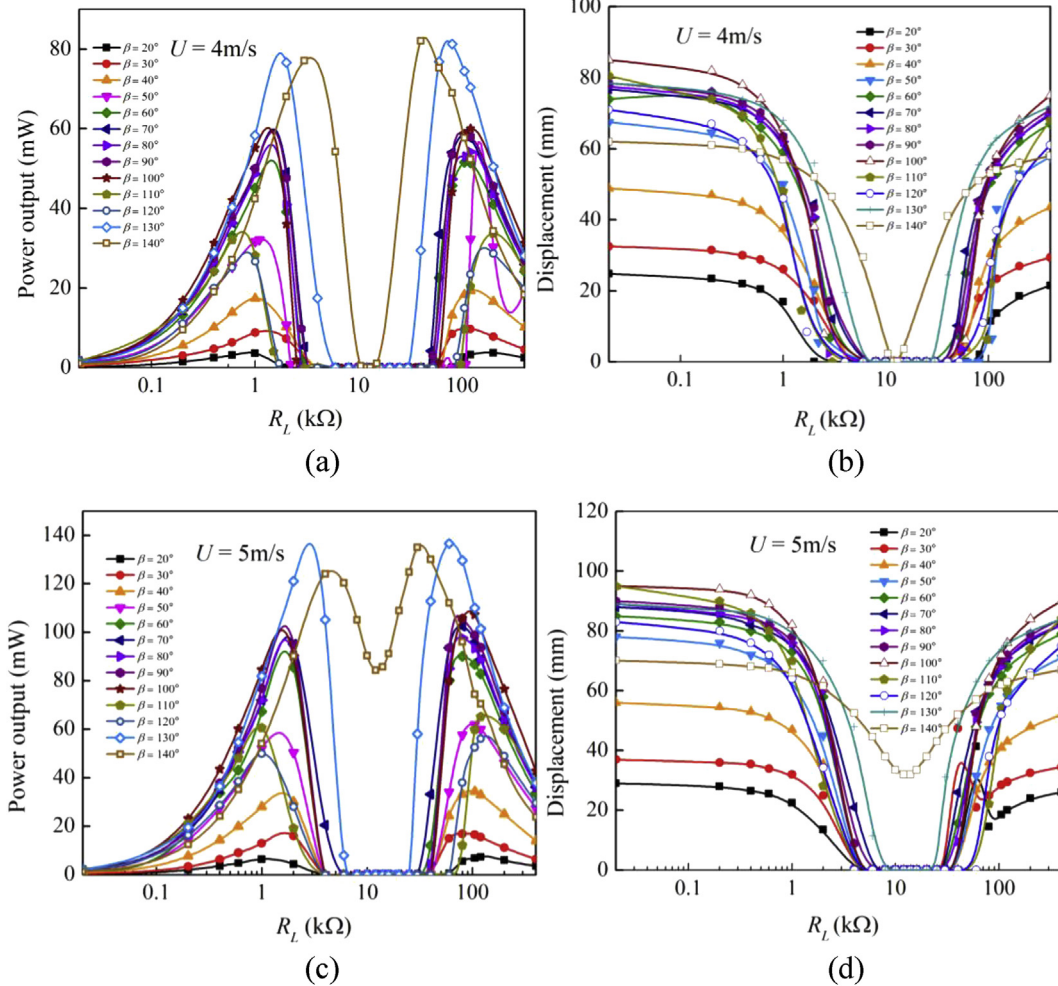


Fig. 14. Comparison of power outputs and displacements of GPEH with different bluff body vertex angles for strong coupling $k_e^2/\zeta = 27.74$: (a) P versus R_L , $U = 4$ m/s, (b) y versus R_L , $U = 4$ m/s, (c) P versus R_L , $U = 5$ m/s, and (d) y versus R_L , $U = 5$ m/s.

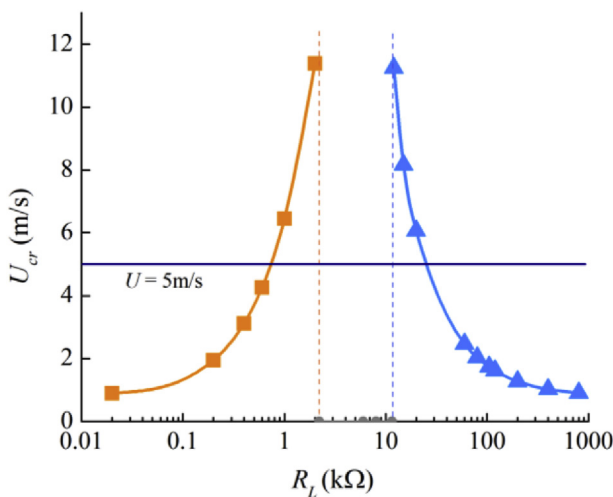


Fig. 15. Variations of threshold wind speed with different R_L for strong electromechanical coupling ($\beta = 130^\circ$).

Meanwhile, it has been determined that the parameter k_e^2/ζ has a great influence on the power generation performance of GPEHs with various interfaces [11,36]. In the present work, a simple

resistor R_L is considered as interface circuit and the influence of R_L and wind speed on the vibration displacement, threshold wind speed and power output is investigated given current weak coupling condition ($k_e^2/\zeta = 2.78$). Fig. 12 compares the peak displacement and threshold speed of the GPEH with $\beta = 130^\circ$ at different R_L . The difference between the displacement responses for different R_L is not evident as depicted in Fig. 12(a). The threshold speed has minor variation given different R_L , as shown in Fig. 12(b). It can be seen that the GPEH is most difficult to gallop at $R_L = 105\text{--}120$ kΩ, where $U_{cr} = 1.31$ m/s. However, in general, the gap between the threshold galloping speeds for different R_L is not large. Fig. 13 shows the power output of the GPEH with different R_L . It is noted that the growth rate of power increases as R_L going up to 105–120 kΩ. Then it declines when R_L further increases. Thus, with a weak coupling configuration, the optimal load resistance is around 105–120 kΩ.

5.2. Effect of bluff body vertex angles and strong electromechanical coupling

In order to further analyze the influence of electromechanical coupling strength on GPEH with different vertex angles, we set the coupling strength at $k_e^2/\zeta = 27.74$ by increasing χ and C_p by ten times simultaneously.

The responses of tip displacement and average power output for

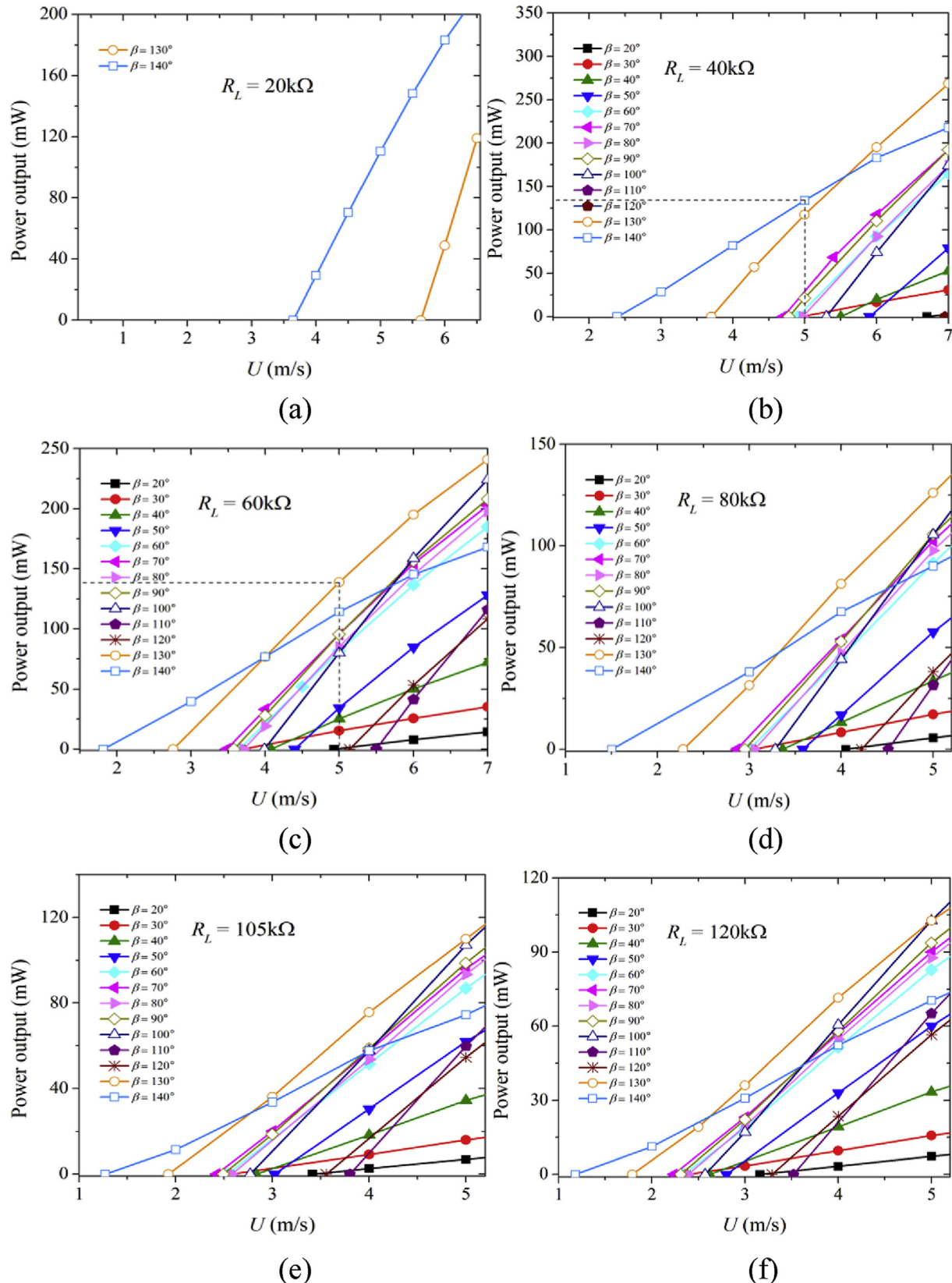


Fig. 16. Comparison of power outputs of GPEH versus U with different bluff body vertex angles for strong electromechanical coupling $k_e^2/\zeta = 27.74$. (a–j) $20\text{k}\Omega, 40\text{k}\Omega, 60\text{k}\Omega, 80\text{k}\Omega, 105\text{k}\Omega, 120\text{k}\Omega, 200\text{k}\Omega, 400\text{k}\Omega, 600\text{k}\Omega$, and $800\text{k}\Omega$.

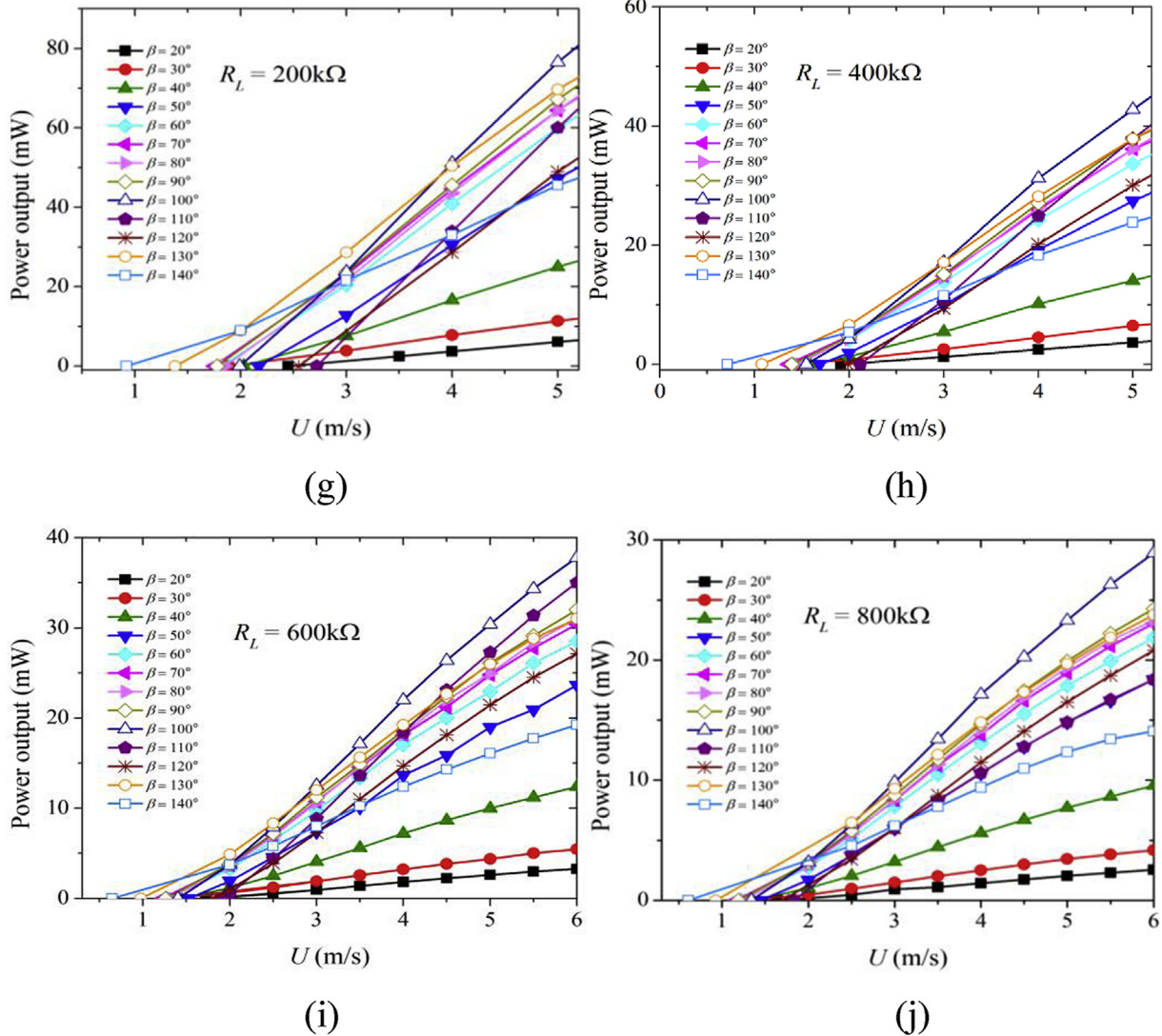


Fig. 16. (continued).

different R_L for GPEH with different β are shown in Fig. 14. From Fig. 14(a) and (c), it is obvious that there are two power peaks with almost equal magnitude and a valley of power appears in this strong coupling configuration, which is consistent with observations by Zhao and Yang [36]. Fig. 14(b) and (d) shows the corresponding valley of displacement amplitude. The valley of the power output is associated with the valley of the displacement. From the comparison of Fig. 14(a–d), when the wind speed increases, the valley region of the power or the displacement shrunk for all bluff bodies.

Fig. 15 shows the impact of R_L on threshold wind speed in the strong coupling system ($\beta = 130^\circ$). For $R_L = 0.02\text{k}\Omega$ to around $2.2\text{k}\Omega$, the threshold has increased from 0.9 m/s to 11.38 m/s . In the region from $2.2\text{k}\Omega$ to $11.6\text{k}\Omega$, galloping could not occur in the considered range of wind speed because of the high backward electrical damping effect under strong coupling condition. For $R_L = 12\text{k}\Omega$ to around $800\text{k}\Omega$, threshold speed decreases from 11.25 m/s to 0.91 m/s .

Further parametric study is conducted to investigate the influence of the vertex angle in the strong coupling configuration with different load resistances in Fig. 16. Based on the previous results in Fig. 15, to avoid the power valley regions for all configurations, a

series of load resistances ($R_L \geq 20\text{k}\Omega$) have been employed. Ten values of R_L have been investigated here to decide the preferred vertex angle and load resistance.

It is noted that the threshold wind speed is more sensitive to the vertex angle for a low resistance R_L (e.g., Fig. 16(b)) than a high resistance (e.g., Fig. 16(j)). This is also reflected in Fig. 15, where the threshold speed at low resistance on the right hand side of the valley changes violently as compared to a higher load resistance. For a low resistance, such as $20\text{--}40\text{k}\Omega$, the bluff body with $\beta = 130^\circ$ and 140° gives similar power output as shown in Fig. 16(a). Most β require very high wind speed to initiate galloping, and are unable to generate power in the considered wind speed range except 130° and 140° (Fig. 16(a)). However, the significant difference in the threshold speed implies that 140° is a better choice to ensure both low threshold speed and high power output. With the increase of R_L , the threshold speeds get clustered for different vertex angles.

In addition, the most preferred vertex angle β_m will change with R_L . For example, for $R_L = 120\text{k}\Omega$, $\beta = 130^\circ$ gives the highest power output at 5 m/s , which is much higher than that of $\beta = 140^\circ$. Though the threshold speed is not the lowest, compromising the power output and threshold speed implies that $\beta = 130^\circ$ is the preferred choice. With the further increase of R_L , β_m is reduced. For example,

for $R_L = 400 \text{ k}\Omega$, the threshold wind speeds of various bluff bodies are further clustered. The $\beta = 100^\circ$ gives the highest power at 5 m/s with a slightly increased threshold wind speed as compared to $\beta = 130^\circ$. Hence, $\beta = 100^\circ$ should be regarded as the most preferred vertex angle β_m . In summary, under a strong coupling strength, the most preferred vertex angle β_m varies with the load resistance. This phenomenon differs from that under weak coupling condition, in which $\beta = 130^\circ$ is always the best choice in any cases.

6. Conclusions and future work

This paper investigates the influence of the vertex angle of an isosceles triangle-sectioned bluff body on the performance of GPEH. The empirical aerodynamic force coefficients are calculated using the CFD method based on Opensource C++ platform OpenFOAM, and this work was validated by experimental data in the literature. Subsequently, an aero-electro-mechanical coupled model is established with the aerodynamic force obtained from the CFD results. A parametric study is then conducted to investigate the behavior of GPEH with different vertex angles and electromechanical coupling strengths. The ultimate goal is to determine the most preferred vertex angle β_m for designing efficient GPEH with an isosceles triangle-sectioned bluff body. The main findings are as follows:

- **Aerodynamic force coefficients:** An orthogonal distance regression fitting method is used to obtain the empirical nonlinear aerodynamic force coefficients. For vertex angle $\beta \leq 20^\circ$, the coefficient b_1 is negative and galloping is not possible. Galloping occurs for $\beta = 20^\circ - 140^\circ$. For $\beta > 140^\circ$, the patterns of velocity and vorticity are not sensitive to the incoming wind and thus not good for application in energy harvesting.
- **Influence of electromechanical coupling strength:** In this work, we first use a weak electromechanical coupling ($k_e^2/\zeta = 2.78$) to determine the most preferred vertex angle β_m . With the identified β_m , we investigate the influence of electromechanical coupling strength on the performance of GPEH. The results show that the threshold of galloping first increases and then decreases with the load resistance and given weak coupling strength. However, for strong coupling strength, due to the high backward electrical damping when R_L lies in a specific region, galloping could not happen in the considered range of wind speeds. At the same time, the optimal R_L varies with the coupling strength.
- **Most preferred vertex angle of triangular bluff body:** By compromising the sensitivity of galloping threshold and good capacity of harvesting energy with weak coupling, $\beta = 130^\circ$ is determined to be the most preferred vertex angle β_m within the range of β concerned given an interval of 10° . For strong coupling, β_m changes with R_L in the circuit in different load resistance regions.

It should be mentioned that the present parametric study is performed with the specific electromechanical coupling of our prototyped GPEH with different shaped bluff bodies. Additionally, the comprehensively optimized design and theoretical investigation of the GPEH with triangular bluff body will be attempted in the future work.

Acknowledgement

The authors gratefully acknowledge the support provided by the National Natural Science Foundation of China (No. 51606171) and Seed Funding of University of Technology Sydney (No.2232299).

References

- [1] Zhang L, Dai H, Abdelkefi A, Wang L. Experimental investigation of aerodynamic energy harvester with different interference cylinder cross-sections. Energy 2019;167:970–81.
- [2] Zhou Z, Qin W, Zhu P, Shang S. Scavenging wind energy by a Y-shaped bi-stable energy harvester with curved wings. Energy 2018;153:400–12.
- [3] Kosunalp S. An energy prediction algorithm for wind-powered wireless sensor networks with energy harvesting. Energy 2017;139:1275–80.
- [4] Narendran K, Murali K, Sundar V. Investigations into efficiency of vortex induced vibration hydro-kinetic energy device. Energy 2016;109:224–35.
- [5] Wu Y, Qiu J, Zhou S, Ji H, Chen Y, Li S. A piezoelectric spring pendulum oscillator used for multi-directional and ultra-low frequency vibration energy harvesting. Appl Energy 2018;231:600–14.
- [6] Zhou S, Wang J. Dual serial vortex-induced energy harvesting system for enhanced energy harvesting. AIP Adv 2018;8(7), 075221.
- [7] Chen Z, He J, Liu J, Xiong Y. Switching delay in self-powered nonlinear piezoelectric vibration energy harvesting circuit: mechanism, effects and solution. IEEE Trans Power Electron 2019;34(3):2427–40.
- [8] Zhao X, Cai J, Guo Y, Li C, Wang J, Zheng H. Modeling and experimental investigation of an AA-sized electromagnetic generator for harvesting energy from human motion. Smart Mater Struct 2018;27(8), 085008.
- [9] Wang J, Zhou S, Zhang Z, Yurchenko D. High-performance piezoelectric wind energy harvester with Y-shaped attachments. Energy Convers Manag 2019;181:645–52.
- [10] Petrin I, Gkoumas K. Piezoelectric energy harvesting from vortex shedding and galloping induced vibrations inside HVAC ducts. Energy Build 2018;158: 371–83.
- [11] Zhao L, Yang Y. On the modeling methods of small-scale piezoelectric wind energy harvesting. Smart Struct Syst 2017;19(1):67–90.
- [12] Wang J, Geng L, Zhang M, Zhao G, Zhang M, Zhang Z, et al. Broadening band of wind speed for aeroelastic energy scavenging of a cylinder through buffeting in the wakes of a squared prism. Shock Vib, 2018; 2018, p. 1–14.
- [13] Zhang M, Zhao G, Wang J. Study on fluid-induced vibration power harvesting of square columns under different attack angles. Geofluids 2017;2017(2): 1–18.
- [14] Barrerogil A, Sanzandrés A, Alonso G. Hysteresis in transverse galloping: the role of the inflection points. J Fluid Struct 2009;25(6):1007–20.
- [15] Wang J, Zhao G, Zhang M, Zhang Z. Efficient study of a coarse structure number on the bluff body during the harvesting of wind energy. Energ Source Part A 2018;40(15):1788–97.
- [16] Anagnostopoulos P, Bearman PW. Response characteristics of a vortex-excited cylinder at low Reynolds numbers. J Fluid Struct 1992;6(1):39–50.
- [17] Wang J, Li G, Zhang M, Zhao G, Jin Z, Xu K, et al. Energy harvesting from flow-induced vibration: a lumped parameter model. Energ Source Part A 2018;40(24):2903–13.
- [18] Li S, Yuan JP, Lipson H. Ambient wind energy harvesting using cross-flow fluttering. J Appl Phys 2011;109(2), 026104.
- [19] Kwon SD. A T-shaped piezoelectric cantilever for fluid energy harvesting. Appl Phys Lett 2010;97(16), 164102.
- [20] Simpson BJ, Licht S, Hover FS, Triantafyllou MS. Energy extraction through flapping foils. In: ASME 2008 27th International Conference on Offshore Mechanics and Arctic Engineering; 2008. p. 389–95.
- [21] Kinsey T, Dumas G, Lalande G, Ruel J, Méhat A, Viarouge P, et al. Prototype testing of hydrokinetic turbine based on oscillating hydrofoils. Renew Energy 2011;36(6):1710–8.
- [22] Barrero-Gil A, Alonso G, Sanz-Andres A. Energy harvesting from transverse galloping. J Sound Vib 2010;329(14):2873–83.
- [23] Sirohi J, Mahadik R. Harvesting wind energy using a galloping piezoelectric beam. J Vib Acoust 2012;134(1):011009.
- [24] Sirohi J, Mahadik R. Piezoelectric wind energy harvester for low-power sensors. J Intell Mater Syst Struct 2011;22(18):2215–28.
- [25] Yang Y, Tang L. Equivalent circuit modeling of piezoelectric energy harvesters. J Intell Mater Syst Struct 2009;20(18):2223–35.
- [26] Tang L, Zhao L, Yang Y, Lefevre E. Equivalent circuit representation and analysis of galloping-based wind energy harvesting. IEEE/ASME Trans Mechatron 2014;20(2):834–44.
- [27] Zhao L, Tang L, Liang J, Yang Y. Synergy of wind energy harvesting and synchronized switch harvesting interface circuit. IEEE/ASME Trans Mechatron 2017;22(2):1093–103.
- [28] Bibo A, Abdelkefi A, Daqaq MF. Modeling and characterization of a piezoelectric energy harvester under combined aerodynamic and base excitations. J Vib Acoust 2015;137(3), 031017.
- [29] Zhao L, Yang Y. An impact-based broadband aeroelastic energy harvester for concurrent wind and base vibration energy harvesting. Appl Energy 2018;212:233–43.
- [30] Yang Y, Zhao L, Tang L. Comparative study of tip cross-sections for efficient galloping energy harvesting. Appl Phys Lett 2013;102(6), 064105.
- [31] Alonso G, Meseguer J. A parametric study of the galloping stability of two-dimensional triangular cross-section bodies. J Wind Eng Ind Aerod 2006;94(4):241–53.
- [32] Alonso G, Meseguer J, Pérez-Grande I. Galloping stability of triangular cross-sectional bodies: a systematic approach. J Wind Eng Ind Aerod 2007;95(9): 928–40.

- [33] Spalart P, Allmaras S. A one-equation turbulence model for aerodynamic flows. *La Recherche Aérospatiale* 1994;43(1):5–21.
- [34] Ding L, Bernitsas MM, Kim ES. 2-D URANS vs. experiments of flow induced motions of two circular cylinders in tandem with passive turbulence control for $30,000 \leq Re \leq 105,000$. *Ocean Eng* 2013;72:429–40.
- [35] Tang L, Yang Y. Analysis of synchronized charge extraction for piezoelectric energy harvesting. *Smart Mater Struct* 2011;20(8), 085022.
- [36] Zhao L, Yang Y. Analytical solutions for galloping-based piezoelectric energy harvesters with various interfacing circuits. *Smart Mater Struct* 2015;24(7), 075023.